Radiotherapy and Oncology 215 (2026) 111261

Contents lists available at ScienceDirect

Radiotherapy and Oncology

journal homepage: www.thegreenjournal.com

Original Article

Risk modeling of imaging changes after proton beam therapy for childhood brain tumors

Feline Heinzelmann [a,b,c,*], Sarah Peters [a,d], Annika Quenzer [e], Armin Lühr [b], Steffen Löck [f,g], Stefanie Schulze Schleithoff [a], Sabine Frisch [a], Christian Bäumer [a,b,c,h], Beate Timmermann [a,c,d,h,i]

[a] West German Proton Therapy Centre Essen (WPE), Essen, Germany
[b] TU Dortmund University, Department of Physics, Dortmund, Germany
[c] West German Cancer Center (WTZ), University Hospital Essen, Essen, Germany
[d] Clinic for Particle Therapy, University Hospital Essen, Essen, Germany
[e] Department of Neuroradiology, University Hospital Wuerzburg, Wuerzburg, Germany
[f] OncoRay National Center for Radiation Research in Oncology, Faculty of Medicine and University Hospital Carl Gustav Carus, TUD Dresden University of Technology, Helmholtz-Zentrum Dresden-Rossendorf, Dresden, Germany
[g] Department of Radiotherapy and Radiation Oncology, Faculty of Medicine and University Hospital Carl Gustav Carus, TUD Dresden University of Technology, Dresden, Germany
[h] German Cancer Consortium (DKTK), Essen, Germany
[i] University of Duisburg-Essen, Faculty of Medicine, Essen, Germany

ARTICLE INFO

Keywords:
Proton beam therapy (PBT)
Brain cancer
Childhood brain tumors
Normal tissue complication probability (NTCP)
Imaging changes
Adverse effects
Relative biological effectiveness (RBE)
Linear energy transfer (LET)
Periventricular region (PVR)
Brainstem

ABSTRACT

Background and purpose: In childhood brain tumors, minimizing long-term side effects of cancer therapy is a critical objective. Radiation-related imaging changes (ICs), indicative of potential radionecrosis, remain an area of active investigation in proton beam therapy (PBT). This study aimed to identify and correlate post-therapeutic ICs and radio-biological and dosimetric factors, including linear energy transfer (LET) and variable relative biological effectiveness (RBE), as well as clinical factors.

Materials and methods: A 3:1 matched-pair cohort of 93 pediatric PBT patients from a register study was retrospectively analyzed. The cohort comprised various brain tumor entities, with follow-up MRI data available up to 14 months post-treatment. Potential clinical risk factors for therapy-induced ICs in pediatric brains were analyzed using logistic regression at both patient and voxel levels. Dosimetric parameters were evaluated for the entire brain, periventricular region (PVR), and brainstem.

Results: A total of 15 cases with post-therapeutic ICs from various childhood tumor entities were identified and localized in the brainstem, the PVR, and other brain regions. At the voxel level, the key predictor linked to increased IC probability was the product of dose D and proton dose-averaged LETd $(D \cdot \mathrm{LETd}_{\mathrm{proton}})_{\sigma=6\ \mathrm{mm}}$, excluding voxels below 5 Gy (RBE). The Gaussian filtering with a standard deviation σ of 6 mm served as a practical approach to account for spatial uncertainties. At the patient level, the median dose ($D_{50\%}$) within the volume of the healthy brain receiving more than 20 Gy (RBE) was most significant.

Conclusion: The identified univariate voxel- and patient-level risk factors provide a foundation for predicting post-therapeutic ICs in pediatric CNS tumor patients treated with PBT. Our findings contribute to refining risk prediction models and optimizing treatment planning strategies, ultimately aiming to minimize long-term radiation-induced effects in pediatric brain tumor patients.

* Corresponding author at: Universitätsklinikum Essen Westdeutsches Protonentherapiezentrum Essen (WPE) gGmbH, Hufelandstraße 55, 45147 Essen, Germany; TU Dortmund University, August-Schmidt-Straße 1, 44227 Dortmund, Germany

E-mail addresses: feline.heinzelmann@tu-dortmund.de (F. Heinzelmann), sarah.peters@uk-essen.de (S. Peters), quenzer_a1@ukw.de (A. Quenzer), armin.luehr@tu-dortmund.de (A. Lühr), steffen.loeck@oncoray.de (S. Löck), stefanie.schulze-schleithoff@uk-essen.de (S.S. Schleithoff), sabine.frisch@uk-essen.de (S. Frisch), christian.baeumer@uk-essen.de (C. Bäumer), beate.timmermann@uk-essen.de (B. Timmermann).

https://doi.org/10.1016/j.radonc.2025.111261
Received 5 May 2025; Received in revised form 15 October 2025; Accepted 27 October 2025
Available online 3 November 2025

Introduction

Radiotherapy is an essential component of oncology treatment for various childhood brain tumors [1]. Particularly, proton beam therapy (PBT) plays an increasing role because of its unique dose deposition [2]. The low entrance dose and the sharp distal fall-off of PBT fields are considered particularly beneficial for pediatric patients, who represent the most vulnerable patient group. To improve long-term outcomes and increase life expectancy, it is crucial to minimize therapy-related adverse effects and preserve cognitive function. Emerging data increasingly support the low toxicity of PBT [3–12].

Radiation-induced imaging changes (ICs) can occur in brain tumor patients, arising after both proton and photon radiotherapy [13–18]. While many ICs observed after PBT remain asymptomatic and may resolve spontaneously, some patients develop marked toxicities requiring medical intervention [19]. Specifically, brainstem necrotic lesions necessitate immediate intervention, as even minor lesions can cause rapid, life-threatening deterioration due to its critical role in vital autonomic functions [20].

Tissue changes following cancer treatment are commonly observed on follow-up magnetic resonance imaging (fuMRI), namely as T1 contrast enhancements and T2 hyper- and hypo-intensities [21–24]. Although ICs are also observed after photon therapy, multiple studies [26–28] attribute their incidence in PBT at the distal end of the proton track, where the linear energy transfer (LET) and relative biological effectiveness (RBE) increase [34]. When protons are delivered with a low dose per fraction to brain tissue combined with low photon fractionation sensitivity ratios $(\alpha/\beta)_x$, the effective RBE rises, potentially increasing the risk of ICs [29,30]. However, some studies could not identify LET-associated toxicity [22,31]. Considering the scarcity of clinical reports and the multifactorial nature of the effect, a clear picture has not yet emerged.

Recent studies have provided evidence of dose- and LET-dependent IC formation in PBT patients [25,26,28,32,33,34–36]; several of these studies have further demonstrated that ICs additionally correlate with ventricular proximity [25,26,34,35]. To quantify the risk of IC formation, these studies introduced normal tissue complication probability (NTCP) models incorporating these correlated risk factors. As most existing NTCP models have been primarily established for adult glioma patients, or solely for pediatric ependymoma patients treated with PBT [32,37], their applicability to childhood central nervous system (CNS) tumors remains uncertain.

This study aims to extend NTCP modeling to pediatric CNS tumor patients, investigating the correlations between post-therapeutic ICs and key dosimetric and anatomical predictors—LET, RBE, radiosensitivity of the periventricular region (PVR) and brainstem—as well as clinical predictors. A novel aspect of this monocentric study is the inclusion of diverse tumor entities, complex pencil-beam scanning (PBS) treatment plans involving multiple target volumes, and plan adaptations based on second CT scans.

Material and methods

Study design

In total, 93 patients ($\leq$ 18 years) with malignant brain tumors irradiated with PBS at the West German Proton Therapy Centre in Essen between June 2014 and September 2019 were included in this retrospective study. Patients were enrolled in the prospective registry study (KiProReg; German Clinical Trials Register: DRKS-ID: DRKS00005363) after the formal consent of their legal guardian(s). Treatment and dose prescription for each patient followed national and international guidelines for the respective tumors.

Originally, the treatment plans were created with the treatment planning system RayStation© (RS) (v4.5.1.14, v4.7.2.5, v5.0.2.35, v6.1.1) using the pencil beam algorithm. A re-simulation was performed using the research version of RS (version 12.0.130.30) with a built-in Monte Carlo (MC) dose engine (version v5.3), enabling the computation of LET and variable RBE. The dose distributions were calculated with a maximum statistical uncertainty of 0.5 %, defined as the average standard uncertainty over all voxels having a dose exceeding 50.0 % of the maximum dose per field. The dose grid resolution matched the CT grid resolution—$1.17 \times 1.00 \times 1.17\,\mathrm{mm}^3$ or $1.17 \times 2.00 \times 1.17\,\mathrm{mm}^3$ for craniospinal irradiations. For a CT grid resolution less than 1 mm, the minimum available dose grid resolution of the used RS version was selected: $(1.00 \times 1.00 \times 1.00\,\mathrm{mm}^3)$.

The LETd was calculated by the unrestricted LET_∞ in water normalized to unit density [38] considering either LET from primary and secondary protons, or LET from primary protons and secondary ions (protons, deuterons and alphas). Since several patients received multiple treatment plans—such as sequential boosts, adjustments to the planning target volume (PTV), or organ-at-risk (OAR) blocking—an effective dose-weighted LETd was calculated for each voxel across all sequential plans. Assuming LETd is additive, this was achieved by determining the dose-weighted average of the dose-averaged LET from each individual plan, as described further in the Supplementary Eq. (A.1).

To evaluate the impact of a variable RBE, dose distributions were calculated using different phenomenological models [39–42], which differ in the definition of $\mathrm{RBE}_{\mathrm{min}}$ and $\mathrm{RBE}_{\mathrm{max}}$ [43], as well as RBE models scaling linearly with LET [34,44]. All phenomenological models depend on LETd and $(\alpha/\beta)_x$ [45], which was set to 2 Gy for normal brain tissue voxels [46].

The modeling of normal brain tissue only considered voxels receiving > 1 Gy (RBE = 1.1). Analyses were restricted to the brain mask after excluding voxels within the gross tumor volume (GTV), defined as the resection cavity (if present) plus any residual tumor, and the ventricular system (VS). Potentially tumor-infiltrated margins surrounding the GTV were included, as they are expected to consist primarily of normal brain tissue at the dose grid resolution.

For the evaluation, additional Gaussian-filtered dose and LETd distributions with a standard deviation of $\sigma = 3$ mm and $\sigma = 6$ mm were included to account for spatial uncertainties, e.g., of the processing of FU scans, including ROI segmentation and their image registrations onto the planning CTs (pCTs). This filtering also aimed to mitigate uncertainties inherent to the treatment planning process, such as those arising from simulations, including positioning and range uncertainties and their sensitivity to tissue heterogeneities (see further calculation details in Eq. (A.2)). The dose-dependent variables were also corrected for Equivalent Dose in 2 Gy (RBE) Fractions (EQD2) (see Eq. (A.3)) to standardize dose–response relationships across non-uniform fractionation schemes and to allow for possible comparisons of existing models with standard 2 Gy (RBE) fractions. Here, 'Gy (RBE)' refers to both variable and constant RBE-weighted dose variants, denoted accordingly.

Patient cohort and follow-up characteristics

FU consultations with a radiation oncologist were scheduled at three months after PBT and annually thereafter. Symptoms and side effects were documented and classified according to the Common Terminology Criteria for Adverse Events (CTCAE) Version 4.0 at three key time points: before PBT initiation, weekly during PBT, and at FU. Imaging FU was conducted at the treating medical facility according to local standards, with the first MRI performed within three months after PBT and subsequent scans at regular intervals thereafter every three to six months. The imaging protocol typically included T1-weighted images (T1WI), T2-weighted images (T2WI), diffusion-weighted images (DWI), susceptibility-weighted images (SWI), T2 fluid-attenuated inversion recovery sequence (FLAIR), and T1WI after contrast media application (T1wCE). To identify ICs, retrospective patient screening was conducted based on a previously published methodology [47], according to which radiology reports from the first 14 months post-PBT were reviewed for

newly emerging ICs using a predefined set of keywords. Identified IC cases in the reports underwent external neuroradiology reference evaluation and were graded according to Fouladi et al. [48].

Screened registry-study patients were excluded if they had received prior photon irradiation, had primary spinal tumors or were treated with uniform scanning. In fifteen screened cases, ICs were confirmed in fuMRI. Symptomatic patients reported headache, visual impairment, cranial nerve disorders, dysphagia, and dyspnea. To ensure a robust study design and comparability, particularly regarding tumor entity, the reference non-IC cohort was selected to maintain an entity ratio of at least 3:1 relative to IC cases, supplemented by additional tumor entities. The final cohort comprised 93 pediatric patients. Table 1 and Table A1 provide an overview of patient demographics, tumor entity distribution, treatment, and IC characteristics. Note that before, during, or after PBT, patients could have received chemotherapy.

Imaging findings and periventricular region

After assessment by a reference radiologist, the largest IC in each case was manually contoured on fuMRI, provided it was confirmed as non-tumor progression. Contours were then co-registered to the pCT using a deformable-registration workflow within RS, which combines rigid and deformable registration with validation steps in between (see Supplementary Fig. A1).

To investigate the IC–PVR association reported in [25–27], the VS were manually delineated on the pMRI based on the pediatric germ cell tumor (GCT) contouring atlas for PBT [49] and then mapped onto the pCT (see Fig. A1). The PVR was defined as the 4-mm rim of the mapped VS contour without the prepontine cistern [25,26], which is illustrated in Fig. 1 as an example for a patient with an IC finding.

Statistical analysis

Risk factors for IC occurrence following PBT were assessed via uni- and multivariate logistic regression analyses at both patient and voxel level, using the logistic function $\mathrm{NTCP} = 1/\left(1+\exp\left(-\vec{x}\cdot\vec{\beta}\right)\right)$. The patient-level analysis was performed to calculate NTCP for the endpoint IC occurrence per patient. The voxel-level models predict the IC location for every voxel in the pCT. Here, dose grid voxels within an IC were labeled as 1 (affected), others as 0 (non-affected). To enhance the validity of the analysis, voxels below 1 Gy (RBE = 1.1) were excluded.

Given the challenge of imbalanced data, repeated cross-validation (CV) was used to yield robust model performance estimates, applying a 3-fold stratified CV with 333 repeats at the patient level and a 10-fold stratified CV with 3 repeats at the voxel level. Intercepts, coefficients, and confidence intervals (CI) were averaged across the training sets of each fold for an overall model summary. The statistical significance of predictors was calculated by averaged z-values from the Wald test. Model performances were quantified by the area under the ROC (receiver-operating characteristic) curve (AUC) calculated across all test data sets. The final NTCP model was selected based on the highest mean cross-validated AUC ($\mathrm{AUC}_{\mathrm{CV,mean}}$).

For the patient-level model, dose-volume histogram (DVH) parameters within the whole brain, the brainstem, and the PVR were evaluated. The parameters analyzed were D_X (dose received by X% of the structure's volume) for both constant and variable RBE models, L_X (LETd for X% of the volume), evaluated at $X = [1\%, 2\%, 5\%, 50\%, \mathit{mean}]$, and the generalized equivalent uniform dose (gEUD) [50] with $a = 1$ to 20 in steps of 1. These parameters were calculated for a set of discrete dose thresholds [1,2,3,4,5,10,20,30,40,50,54] Gy (RBE = 1.1) to capture a comprehensive spectrum of dose–response relationships.

Voxel-wise logistic regression was performed on the patients' brain voxel dataset considering constant RBE-weighted dose ($D(\mathrm{RBE}=1.1)$), variable RBE-weighted doses, LETd, $D(\mathrm{RBE}=1.1)\times$ LETd, and binary masks for the PVR and brainstem as independent variables. For each dosimetric and LET parameter, including the product of dose and LETd, untransformed, EQD2-corrected, and Gaussian-filtered variants were tested. Each voxel-level model specified its own minimum dose threshold—1, 2, 3, 4, 5, 10, 15, 20, 25, 30, 35, or 40 Gy (RBE = 1.1). All voxels receiving less than that model–specific threshold were excluded from the analysis, employing smaller intervals at lower doses to capture finer variations and larger intervals in the higher dose range to account for reduced sensitivity.

Results

In the 15 identified cases, the ICs reached their maximal extent at a median of 4.53 months after the completion of PBT. The observed IC volume exhibited a large variability with a median volume of 0.01 cm^3 and a mean volume of 2.23 cm^3 from 186 IC incidents within 15 cases. ICs were irregularly distributed throughout the brain and the treatment fields but were mainly found in high dose regions (>40 Gy (RBE = 1.1)) adjacent to the PTV, at the edge of the GTV, or resection cavity, with overlaps with the PVR and brainstem. Using a dose cutoff of 1 Gy (RBE = 1.1), 59.4% of the IC voxels received doses exceeding 40 Gy (RBE = 1.1). Among the voxels receiving $\leq$ 40 Gy (RBE = 1.1), 71.5% exhibited LETd values above 2.5 keV/µm (see Supplementary Fig. A2). Additionally, ICs of two patients were distributed throughout the entire brain. In two other cases, ICs occurred outside the high-dose range with low LET values.

Table 2 shows a comparison of the model performances using logistic regression. For the highest–AUC NTCP regression models, Table 3 lists the logistic regression coefficients and intercepts ($\vec{\beta}$), along with the classification thresholds optimized using Youden's index (see Eq. (A.4)).

The most predictive parameter for the univariable voxel-level analysis, $(D\cdot \mathrm{LETd}_{\mathrm{proton}})_{\sigma=6\ \mathrm{mm}}$ with an RBE weight of 1.1, was correlated to IC with an $\mathrm{AUC}_{\mathrm{CV,mean}}$ value of 0.807 and 0.805 when using a threshold of 5 and 10 Gy (RBE = 1.1), respectively (see Table 2). The highest spatial IC discrimination was achieved by a combination of the predictors $D_{\sigma=6\ \mathrm{mm}}$, $(D\cdot \mathrm{LETd}_{\mathrm{proton}})_{\sigma=6\ \mathrm{mm}}$, PVR, and brainstem in a multivariate voxel-wise analysis ($\mathrm{AUC}_{\mathrm{CV,mean}} = 0.813$).

For patient-wise univariate NTCP models, $D_{50\%}$ (brain) calculated with the constant RBE model and a dose cutoff of 20 Gy (RBE = 1.1) emerged as the most predictive dosimetric surrogate with an $\mathrm{AUC}_{\mathrm{CV,mean}}$ value of 0.820 (see Table 2 and Fig. 2). Variable RBE models did not improve $\mathrm{AUC}_{\mathrm{CV,mean}}$ values for $D_{50\%}$ (brain) with the 20 Gy (RBE = 1.1) dose cutoff: 0.783–0.801, with 2.5th percentiles of the confidence intervals (CIs) > 0.6 and coefficients being significant by the Wald test (p-value $\leq$ 0.05). At the patient level, the most prominent factor identified by Eulitz et al. [34]—PVR's gEUD_{11} using the RBE model from [34] and a dose cutoff threshold of 1 Gy (RBE = 1.1)—yielded an $\mathrm{AUC}_{\mathrm{CV,mean}}$ of 0.720 (95 % CI: [0.510, 0.930]). Our patient-wise results indicate that within the PVR, LET-volume histogram (LVH) parameters $L_{2\%,\mathrm{proton}}$ and $L_{5\%,\mathrm{proton}}$ become more prominent predictors of the endpoint at the higher dose cutoff thresholds (> 40 Gy (RBE = 1.1)) than dose-related volume parameters. When using a dose threshold of 50 Gy (RBE = 1.1), the PVR contour yielded the highest $\mathrm{AUC}_{\mathrm{CV,mean}}$ scores for these LVH parameters with the corresponding values being 0.774 [0.595, 0.954] and 0.774 [0.590, 0.958], respectively, highlighting the relevance of these predictors in regions receiving elevated doses.

The 95 % CIs for all tested clinical predictors included 0.5; however, age at PBT start and the prescribed dose demonstrated the strongest

Table 1

Baseline patient demographics, clinical and treatment characteristics of the pediatric central nervous system tumor cohort. For each variable, group-specific medians or counts and the corresponding two-sided p-values are shown. Each *p*-value is the probability, assuming no true difference between IC and non-IC patients, of observing a test statistic as extreme as or more extreme than the one obtained. Significant *p*–values ($p < 0.05$) are marked in bold.

Characteristics	All patients ($n = 93$)	IC patients ($n = 15$)	Non-IC patients ($n = 78$)	*p*-value
	Median (Min – Max)			
General				
Age at PBT (y)	8.69 (0.94–17.40)	3.89 (1.21–16.96)	10.12 (0.94–17.40)	**0.047** (M†)
CTV (cm^3)	53.42 (8.00–1893.23)	68.00 (18.13–1536.83)	51.29 (8.00–1893.23)	0.774 (M)
PVR (cm^3)	97.66 (59.76–174.26)	91.14 (70.81–110.74)	98.56 (59.76–174.26)	0.055 (M)
Treatment				
Prescription dose (Gy (RBE = 1.1))	54.00 (24.00–72.00)	57.60 (54.00–59.40)	54.00 (24.00–72.00)	**0.034** (M)
Fraction dose (Gy (RBE = 1.1))	1.80 (1.00–5.00)	1.80 (1.80–1.80)	1.80 (1.00–5.00)	0.133 (M)
Number of fields	3 (2–5)	2.5 (2–4)	3 (2–5)	0.225 (M)
	Number of patients (%)			
Gender				
Male	56 (60.22)	8 (53.33)	48 (61.54)	0.902 (χ^2††)
Female	37 (39.78)	7 (46.67)	30 (38.46)	
Tumor type				
ATRT	8 (8.60)	2 (13.33)	6 (7.69)	
CPT	2 (2.15)	/	2 (2.56)	
Craniopharyngioma	11 (11.83)	1 (6.67)	10 (12.82)	
Ependymoma	27 (29.03)	8 (53.33)	19 (24.36)	
ETANTR/ETMR	3 (3.23)	1 (6.67)	2 (2.56)	
GCT	13 (13.98)	/	13 (16.67)	
Glioma†††	14 (15.05)	2 (13.33)	12 (15.38)	
Medulloblastoma	13 (13.98)	1 (6.67)	12 (15.38)	
Neuroblastoma	1 (1.08)	/	1 (1.28)	
RGNT	1 (1.08)	/	1 (1.28)	
Supratentorial	46 (49.46)	9 (60.00)	37 (47.44)	0.328 (FFH††††)
Infratentorial	35 (37.63)	6 (40.00)	29 (37.18)	
Both	12 (12.90)	/	12 (15.38)	
WHO grade				
I	17 (18.28)	1 (6.67)	16 (20.51)	
II	8 (8.60)	/	8 (10.26)	
III	27 (29.03)	9 (60.00)	18 (23.08)	
IV	26 (27.96)	4 (26.67)	22 (28.21)	
Unknown/ inapplicable†††††	15 (16.13)	1 (6.67)	14 (17.95)	
Higher WHO grade III-IV (without inapplicable cases)	53 (56.99)	13 (24.53)	40 (51.28)	**0.030** (F†††††)
Primary oncologic and adjunct interventions				
Sx (yes)	77 (82.80)	14 (93.33)	63 (80.77)	0.454 (F)
Bx (yes)	17 (18.28)	4 (26.67)	13 (16.67)	0.287 (F)
VP shunt (yes)	14 (15.05)	2 (13.33)	12 (15.38)	1.0 (F)
CTx (yes)	58 (62.37)	9 (15.52)	49 (62.82)	1.0 (χ^2)
Prior resection				
None	16 (17.20)	1 (6.67)	15 (19.23)	
R0	32 (34.41)	5 (33.33)	27 (34.62)	
R1	6 (6.45)	4 (26.67)	2 (2.56)	
R2	39 (41.94)	5 (33.33)	34 (43.59)	
Macroscopic tumor present at PBT (yes)	55 (59.14)	6 (40.00)	49 (62.82)	0.321 (χ^2)
IC characteristics				
	Median (Min – Max)			
Volume (cm^3)††††††	0.00 (0.00–222.04)	0.01 (0.00–222.04)	/	
Maximal extent after PT end (d)	0 (0–287)	138 (41–287)	/	
	Number of patients (%)			
CTCAE symptoms	6 (6.45)	6 (40.00)	/	
IC Fouladi grading				
1	3 (3.23)	3 (20.00)	/	
2	5 (5.34)	5 (33.33)	/	
3	2 (2.15)	2 (13.33)	/	
4	5 (5.34)	5 (33.33)	/	

Abbreviations: IC, imaging change; *n*, number; PBT, proton beam therapy; y, years; M, Mann–Whitney U; CTV, clinical target volume; PVR, periventricular region; RBE, relative biological effectiveness; χ^2, chi-squared test; FFH, Fisher–Freeman–Halton exact test; ATRT, atypical teratoid rhabdoid tumor; CPT, choroid plexus tumor; ETANTR/ETMR, embryonal tumor with abundant neuropil and true rosettes; GCT, germ cell tumor; RGNT, rosette-forming glioneuronal tumors; Sx, surgery; Bx, biopsy; F, Fisher's exact test; VP, ventriculoperitoneal; CTx, chemotherapy; d, days; CTCAE, Common Terminology Criteria of Adverse Events.

† Mann–Whitney U median test for continuous data.

[††] χ^2–Test of independence as large–sample approximation for any contingency table (2 × 2 or R × C) with categorical/binary data when all expected cell counts ≥ 5.
[†††] Gliomas included astrocytomas, gangliogliomas, and glioblastomas.
[††††] Fisher–Freeman–Halton test for multi-categorical data with cell counts < 5.
[†††††] Inapplicable in case of GCTs and unknown in case of craniopharyngiomas.
[††††††] Fisher's exact test for 2 × 2 contingency table with categorical/binary data if any expected cell counts is < 5.
[†††††††] The volume is the total volume, i.e. without corrections due to fewer voxels after the dose thresholds have been applied.

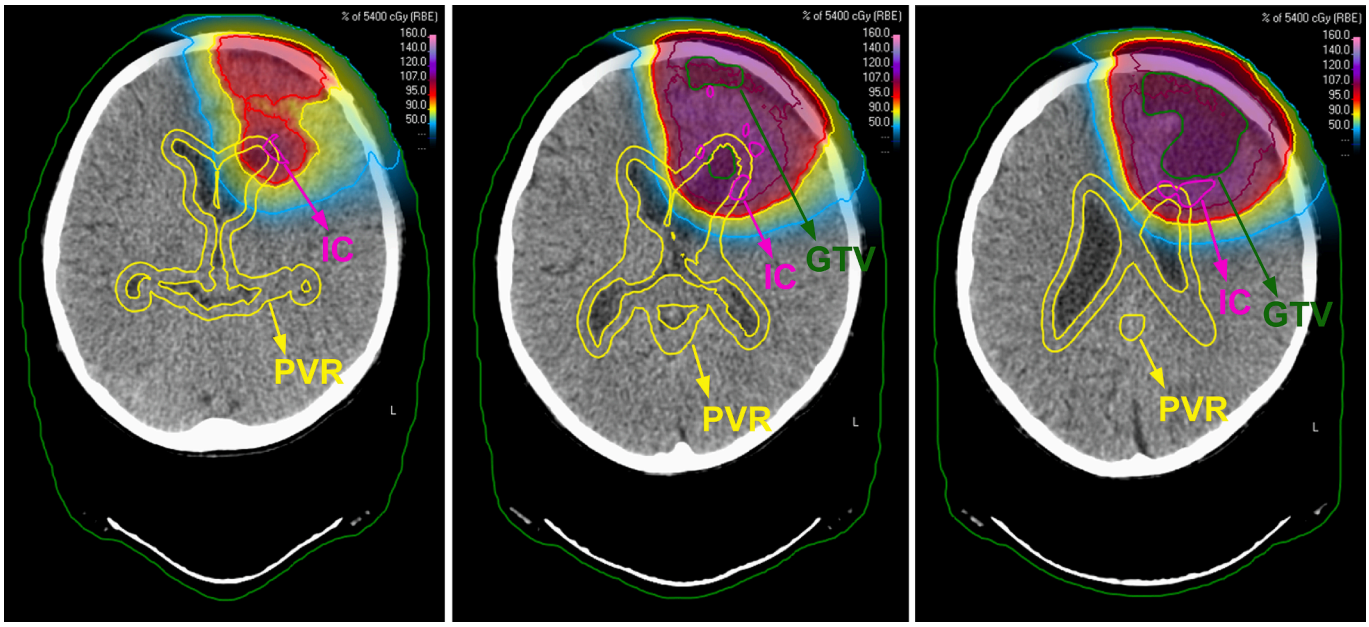

Fig. 1. Planning CT with a mapped dose distribution in Gy (RBE = 1.1) for an example patient with an imaging change in magenta, the PVR in yellow, and the GTV in green. In the color bar, 100% represents the prescription dose of 54 Gy (RBE = 1.1). (For interpretation of the references to color in this figure legend, the reader is referred to the web version of this article.)

predictive power, with $AUC_{CV,mean}$ values above 0.6 (Table 2). The corresponding model coefficients are provided in Table A2 for reference.

Across patient-wise and voxel-wise models, coefficients were uniformly positive for dose, LETd, brainstem, and PVR.

Discussion

In the present study, 15 pediatric brain tumor patients with ICs observed on fuMRI were analyzed in a cohort of 78 cases without ICs. Based on this cohort, the voxel-level logistic regression model of the Gaussian-filtered dose-LETd product $(D \cdot \mathrm{LETd}_{\mathrm{proton}})_{\sigma=6\ \mathrm{mm}}$ with a dose threshold of 5 Gy (RBE = 1.1) was the best performing cross-validated model with a mean AUC of 0.807 [0.805, 0.809]. The most predictive parameter for a univariate patient-wise NTCP model was $D_{50\%}$ within the brain for a dose threshold of 20 Gy (RBE = 1.1.) with an $AUC_{CV,mean}$ of 0.820 [0.648, 0.992].

There are uncertainties at various processing stages, e.g., the accurate detection, localization, and the dosimetric analysis of ICs. A major source of spatial uncertainty affecting dosimetric accuracy arises from proton range uncertainty. Additionally, registration uncertainties—particularly in multimodal imaging (e.g., MRI-to-CT registration)—play a crucial role in the spatial correlation of ICs with dosimetric and anatomical factors, directly impacting spatially-resolving NTCP models. These uncertainties stem from:

- differences in image contrast, intensity, resolution, slice thickness, noise characteristics, artifacts, and patient positioning;
- anatomical changes due to patient growth, brain atrophy, or ventricular deformation during the FU period.

The analysis in the spatial domain is further exacerbated by the limited number of fuMRI scans, which were acquired only at distinct time points, thereby restricting the temporal resolution of IC development. As a consequence, the spatial origin of ICs becomes blurred over time. Differences in resolution between the dose/LETd distribution grid, CT imaging grid, and contour data introduce additional spatial uncertainties, affecting the accuracy of dosimetric-response relationships. Therefore, a spatial smoothing is clearly motivated. Gaussian filtering appears to be an appropriate approach in addressing these spatial uncertainties, as shown by the AUC being highest for Gaussian-filtered distributions. This was also reflected by the *p*-values from the significance tests between each Gaussian-filtered distribution and the respective non-filtered counterpart, supporting their role as robust NTCP model predictors. The treatment plans for the study cohort were created with a 3-5 mm CTV/GTV margin. In some of the evaluated scenarios, the applied Gaussian filtering also accounts for the uncertainty of the dose in space during treatment planning and delivery. Applying a Gaussian filter with $\sigma = 6$ mm results in a spatial blurring effect up to about 12 mm ($k = 2$).

Data-driven models—including those developed in this study—may exhibit increased uncertainty when applied outside the parameter space on which they were trained. Moreover, the limited size and distinct class imbalance of the cohort with various pediatric tumor entities, as well as deficiencies in the clinical screening process inherent to the registry study design, such as the limited FU period of 14 months, pose additional limitations for our modeling approach. Despite an FU window that likely encompasses most early imaging changes, late effects may arise years after therapy. However, using a single predictor from the univariate analysis ensured statistical robustness by reducing the risk of overfitting and minimizing the confounding effects of predictor interactions.

Table 2
Cross-validated area-under the curve (AUC) values for variables with the specification of the dose cutoff threshold in Gy (RBE = 1.1) tested in voxel- and patient-level logistic regression analysis with 10-fold and 3-fold cross-validation to predict image change location and occurrence, respectively.

Model	Variable	Dose threshold (Gy (RBE = 1.1))	$AUC_{CV,voxel\text{-}level}$	
			Mean	95% CI
Voxel-level				
		Univariate analysis		
RBE = 1.1	D	10	0.770	[0.768, 0.773]
	D_{EQD2}	10	0.759	[0.756, 0.761]
	$D_{\sigma=3\ mm}$	**10**	**0.771**	**[0.768, 0.773]**
	$D_{\sigma=6\ mm}$	10	0.768	[0.765, 0.770]
	$D_{EQD2,\sigma=3\ mm}$	10	0.761	[0.759, 0.764]
	$D_{EQD2,\sigma=6\ mm}$	10	0.761	[0.759, 0.763]
WED RBE	D (WED RBE)	10	0.791	[0.789, 0.793]
	$D_{\sigma=3\ mm}$ (WED RBE)	**10**	**0.792**	**[0.790, 0.793]**
	$D_{\sigma=6\ mm}$ (WED RBE)	10	0.787	[0.785, 0.789]
	D_{EQD2} (WED RBE)	10	0.783	[0.780, 0.785]
	$D_{EQD2,\sigma=3\ mm}$ (WED RBE)	10	0.785	[0.783, 0.787]
	$D_{EQD2,\sigma=6\ mm}$ (WED RBE)	10	0.785	[0.783, 0.787]
EUL RBE	D (EUL RBE)	10	0.787	[0.785, 0.789]
	$D_{\sigma=3\ mm}$ (EUL RBE)	**10**	**0.789**	**[0.787, 0.791]**
	$D_{\sigma=6\ mm}$ (EUL RBE)	10	0.787	[0.785, 0.789]
	D_{EQD2} (EUL RBE)	10	0.777	[0.775, 0.779]
	$D_{EQD2,\sigma=3\ mm}$ (EUL RBE)	10	0.782	[0.780, 0.784]
	$D_{EQD2,\sigma=6\ mm}$ (EUL RBE)	10	0.785	[0.783, 0.787]
$LETd_{proton}$	LETd	4	0.723	[0.721. 0.725]
		10	0.707	[0.704. 0.709]
	$LETd_{\sigma=3\ mm}$	4	0.721	[0.722, 0.726]
		10	0.709	[0.707, 0.711]
	$LETd_{\sigma=6\ mm}$	**4**	**0.728**	**[0.726, 0.730]**
		10	**0.713**	**[0.711, 0.716]**
RBE = 1.1, $LETd_{proton}$	$D \cdot$ LETd	10	0.795	[0.793, 0.797]
	$D_{EQD2} \cdot$ LETd	10	0.787	[0.785, 0,789]
	$(D \cdot LETd)_{\sigma=3\ mm}$	5	0.800	[0.798, 0.802]
		10	0.799	[0.798, 0.801]
	$(D \cdot LETd)_{\sigma=6\ mm}$	**5**	**0.807**	**[0.805, 0.809]**
		10	**0.805**	**[0.803, 0.806]**
$LETd_{total}$	LETd	3	0.683	[0.680, 0.685]
		10	0.662	[0.660, 0.664]
	$LETd_{\sigma=3\ mm}$	2	0.685	[0.683, 0.687]
		10	0.664	[0.662, 0.667]
	$LETd_{\sigma=6\ mm}$	**2**	**0.687**	**[0.684, 0.689]**
		10	**0.668**	**[0.666, 0.671]**
RBE = 1.1, $LETd_{total}$	$D \cdot$ LETd	10	0.779	[0.777, 0.781]
	$D_{EQD2} \cdot$ LETd	10	0.770	[0.768, 0.772]
	$(D \cdot LETd)_{\sigma=3\ mm}$	10	0.783	[0.781, 0.784]
	$(D \cdot LETd)_{\sigma=6\ mm}$	**5**	**0.789**	**[0.787, 0.792]**
		10	**0.787**	**[0.785, 0.788]**
ROI mask	PVR	40	0.524	[0.522, 0.526]
		10	0.505	[0.503, 0.506]
	Brainstem	**40**	**0.509**	**[0.507, 0.510]**
		10	**0.505**	**[0.504, 0.506]**
		Multivariate analysis		
RBE = 1.1, $LETd_{proton}$	$D \cdot$ LETd & PVR	10	0.800	[0.798, 0.801]
	$D \cdot$ LETd & brainstem	10	0.797	[0.795, 0.798]
	$D \cdot$ LETd & PVR & brainstem	**10**	**0.802**	**[0.800, 0.803]**
	$(D \cdot LETd)_{\sigma=3\ mm}$ & PVR	10	0.804	[0.802, 0.805]
	$(D \cdot LETd)_{\sigma=3\ mm}$ & brainstem	10	0.801	[0.799, 0.803]
	$(D \cdot LETd)_{\sigma=3\ mm}$ & PVR & brainstem	**10**	**0.806**	**[0.804, 0.808]**
	$(D \cdot LETd)_{\sigma=6\ mm}$ & PVR	5	0.811	[0.808, 0.813]
		10	0.809	[0.808, 0.811]
	$(D \cdot LETd)_{\sigma=6\ mm}$ & brainstem	5	0.808	[0.806, 0.811]
		10	0.807	[0.805, 0.808]

(*continued on next page*)

Table 2 (*continued*)

Model	Variable	Dose threshold (Gy (RBE = 1.1))	$AUC_{CV,voxel\text{-}level}$	
			Mean	95% CI
Voxel-level				
	Univariate analysis			
	$(D \cdot LETd)_{\sigma=6\ mm}$ & PVR & brainstem	**5**	**0.812**	**[0.810, 0.815]**
		10	0.811	[0.810, 0.813]
	D & $D \cdot LETd_{proton}$	10	0.797	[0.795, 0.800]
	D & $D \cdot LETd_{proton}$ & PVR	10	0.801	[0.799, 0.803]
	D & $D \cdot LETd_{proton}$ & brainstem	10	0.798	[0.797, 0.800]
	D & $D \cdot LETd$ & PVR & brainstem	**10**	**0.803**	**[0.801, 0.804]**
	$D_{\sigma=3\ mm}$ & $(D \cdot LETd)_{\sigma=3\ mm}$	10	0.801	[0.799, 0.803]
	$D_{\sigma=3\ mm}$ & $(D \cdot LETd)_{\sigma=3\ mm}$ & PVR	10	0.805	[0.803, 0.807]
	$D_{\sigma=3\ mm}$ & $(D \cdot LETd)_{\sigma=3\ mm}$ & brainstem	10	0.802	[0.801, 0.804]
	$D_{\sigma=3\ mm}$ & $(D \cdot LETd)_{\sigma=3\ mm}$ & PVR & brainstem	**10**	**0.807**	**[0.805, 0.808]**
	$D_{\sigma=6\ mm}$ & $(D \cdot LETd)_{\sigma=6\ mm}$	10	0.807	[0.805, 0.809]
	$D_{\sigma=6\ mm}$ & $(D \cdot LETd)_{\sigma=6\ mm}$ & PVR	10	0.809	[0.808, 0.811]
	$D_{\sigma=6\ mm}$ & $(D \cdot LETd)_{\sigma=6\ mm}$ & brainstem	10	0.807	[0.805, 0.809]
	$D_{\sigma=6\ mm}$ & $(D \cdot LETd)_{\sigma=6\ mm}$ & PVR & brainstem	**10**	**0.813**	**[0.810, 0.815]**
Model	**Variable**	**Dose threshold (Gy (RBE = 1.1))**	**$AUC_{CV,patient\text{-}level}$**	
			Mean	95% CI
Patient-level				
	Univariate analysis			
RBE = 1.1	**$D_{50\%}$ (brain)**	**20**	**0.820**	**[0.648, 0.992]**
	$D_{EQD2,50\%}$ (brain)	20	0.799	[0.603, 0.969]
	$gEUD_2$ (brain)	20	0.798	[0.619, 0.978]
WED RBE	$D_{50\%}$ (brain)	20	0.788	[0.607, 0.969]
EUL RBE	$D_{50\%}$ (brain)	20	0.784	[0.601, 0.968]
Clinical variables	**Age at PBT start (y)**	/	**0.661**	**[0.431, 0.891]**
	Prescribed dose (Gy (RBE =1.1))	/	0.652	[0.388, 0.916]
	Surgery (yes)	/	0.559	[0.436, 0.681]
	CTx after PBT (yes)	/	0.553	[0.314, 0.793]
	Vincristine as concomitant CTx (yes)	/	0.552	[0.373, 0.793]
	Concomitant CTx (yes)	/	0.546	[0.332, 0.760]
	MTX as CTx after PBT (yes)	/	0.527	[0.433, 0.620]
	Vincristine as CTx drug (yes)	/	0.515	[0.284, 0.746]
	Intrathecal CTx (yes)	/	0.511	[0.360, 0.662]
	Bx (yes)	/	0.511	[0.310, 0.712]
	Vincristine as CTx after PBT (yes)	/	0.504	[0.310, 0.700]

Abbreviations: AUC, area under the receiver operating curve; CI, confidence interval; D, dose in Gy (RBE = 1.1) if not further declared; σ = X mm, WED = Wedenberg RBE model [39]; Gaussian-filtering with a standard deviation of X mm; EUL = Eulitz RBE model [34]; $LETd_{proton/total}$, dose-averaged linear energy transfer in keV/µm including primary and secondary protons or including all protons, secondary deuterons and alphas; PVR, periventricular region; D_X, dose of the volume X in % receiving the highest dose; y, years, CTx, chemotherapy; MTX, methotrexate; Bx, biopsy.

Notes: For the voxel-level analysis, the rows corresponding to the highest $AUC_{CV,mean}$ value of each predictor category, which is indicated by a thicker horizontal line, are in bold type. The most predictive patient-level dose-volume-histogram variables calculated within the brain as well as non-dosimetric clinical variables with an $AUC_{CV,mean}$ above 0.5 are shown.

The confidence intervals (CI) are calculated as CI = mean ± 1.96·standard deviation.

Within each modeling approach, voxel–level or patient–level, the model with the highest mean cross-validated AUC achieves the best discrimination. However, because these approaches operate on fundamentally different units of analysis, sample size, IC-class proportion, and spatial autocorrelation, their AUCs are not directly comparable.

For PBT, some studies have reported considerable rates of radiation necrosis [13,59]. In recent years, an increasing number of studies have indicated that radiation-induced brain injuries (RIBIs) are associated with contrast-enhancing lesions observed on fuT1wCE at the time of their first appearance [25,26,34,35]. RIBIs detected on T1wCE can indicate severe tissue damage, with radiation necrosis representing a late-stage manifestation.

We developed risk models for the broader endpoint of ICs, rather than developing an NTCP model specifically for predicting RIBIs based on T1wCE. The obtained models reduce the risk of underestimating lesion size by incorporating ICs at their maximal extent seen on MRI scans—delineated on T2WI, including hyperintensities on T2WI/FLAIR and changes on T1WI/T1wCE. Incorporating multiple imaging sequences may improve the characterization of underlying tissue alterations [24], such as white matter lesions (WMLs). WMLs represent the earliest detectable type of radiation-induced brain injury, first appearing on T2WI or T1WI, prior to the emergence of contrast-enhancing lesions [19].

The relevance of the PVR (as well as the brainstem) was found to be lower in voxel- and patient-based NTCP modeling than in some previous studies which reported, for instance, that incorporating the PVR as a binary input significantly improved discrimination between low- and high-IC-risk regions. This discrepancy may stem from differences in IC characteristics: Eulitz et al. [34] focused on ICs smaller than 150 mm^3, whereas the current study tended to involve larger ICs that were located outside or extended beyond the PVR. It may also be attributed to

Table 3
Coefficient values for the voxel- and patient-level NTCP model with highest cross-validated mean AUC values derived from the 3-fold/10-fold stratified cross-validation using Python packages statsmodels (version 0.14.2) for logistic regression analysis and scikit-learn (version 1.4.2) for cross-validating the data and evaluating the model's performance. The model parameters are incorporated into the NTCP model as follows: NTCP $= 1/(1 + \exp(-\vec{x} \cdot \vec{\beta}))$. Additionally, the classification threshold is listed, allowing for a more accurate assessment of the risk for individual patients/voxels using these models.

Univariate models

Model parameters	Voxel-level with dose threshold of 5 Gy (RBE = 1.1)					Patient-level with dose threshold of 20 Gy (RBE = 1.1)				
	Variable	Mean	95% CI	*p*	OR	Variable	Mean	95% CI	*p*	OR
β_0	Intercept	−6.976	[-6.986, −6.967]	0<.001	0.0009	Intercept	−10.961	[-17.924, 3.998]	0.003	0.000017
β_1	$(D \cdot \mathrm{LETd}_{\mathrm{proton}})_{\sigma=6\ \mathrm{mm}}$ [Gy (RBE = 1.1) keV/μm]	0.0216	[0.0216, 0.0217]	0<.001	1.0219	$D_{50\%,\mathrm{brain}}$ [Gy (RBE = 1.1)]	0.2228	[0.0650, 0.3810]	0.008	1.25
t^*	0.005					0.23				

Multivariate models

Model parameters	Voxel-level with dose threshold of 5 Gy (RBE = 1.1)				
	Variable	Mean	95% CI	*p*	OR
β_0	Intercept	−7.161	[-7.172, −7.149]	0<.001	0.0008
β_1	$D_{\sigma=6\ \mathrm{mm}}$ [Gy (RBE = 1.1)]	0.01127	[0.0109, 0.0117]	0<.001	1.011
β_2	$(D \cdot \mathrm{LETd}_{\mathrm{proton}})_{\sigma=6\ \mathrm{mm}}$ [Gy (RBE = 1.1) keV/μm]	0.0203	[0.02023, 0.0205]	0<.001	1.021
β_3	PVR	−0.575	[-0.587, −0.563]	0<.001	0.563
β_4	brainstem	−0.775	[-0.796, −0.754]	0<.001	0.461
t^*	0.005				
$\kappa = \beta_2/\beta_1$	0.554 [μm/keV]				

Abbreviations: CI, confidence interval; OR, odds ratio; *D*, dose; $\mathrm{LETd}_{\mathrm{proton}}$, dose-averaged linear energy transfer including primary and secondary protons; t^*, best classification threshold; κ, RBE model parameter (see Supplementary Eq. (A.5)).

differences in the cohorts studied. Notably, previous analyses were based on an adult glioma cohort, including Vestergaard et al. (WHO grade 2–4 oligodendroglioma or astrocytoma [35]), Eulitz et al. (WHO grade 2–3 oligoastrocytoma, oligodendroglioma, or astrocytoma [34]), or Bahn et al. (WHO grade 1–2 glioma, not otherwise specified [26]) encompassing patients with a median age of 35 (2–63) y. Adult gliomas primarily occur in deep midline structures [52], and their CTV/PTV contours extend into the PVR, yielding higher periventricular doses than in our cohort and a predominant clustering of ICs within the cerebral hemisphere near the VS. By contrast, childhood brain tumors have a unique location and often a direct anatomical relationship to the brainstem. The thirteen pediatric GCTs, which were particularly located in midline structures adjacent to the VS, may serve as a unique subcohort to test the sensitivity of the PVR. But they do not exhibit any incidence of ICs, despite a median prescription dose of 40.0 Gy (RBE = 1.1) (range: 24.0–54.0 Gy (RBE = 1.1)).

On the one hand, no prominent IC predictors were identified among the tested variable RBE-weighted doses in either voxel-wise or patient-wise analysis. On the other hand, considering the ongoing debate within the PBT community and the absence of a universally accepted variable RBE model [53,54], our findings indicate that selecting a specific model may not be as critical for clinical decision-making. Instead, the data suggest that the combination of dose and LET alone is sufficiently predictive to assess ICs on the voxel level. This would reduce the necessity to decide for an RBE model that encompasses radiobiological aspects including tissue parameters when assessing the risk of post-therapeutic ICs for pediatric cases. However, it underscores the general necessity of recording and reporting dose-averaged LET [53].

In the current study, the dose to the brain plays a prominent role for patient-level NTCP models, regardless of whether a constant RBE, variable RBE or gEUD-based model was used. The quantity $D_{50\%}$(brain), after excluding dose voxels below 20 Gy (RBE = 1.1), provides a robust measure for the dose distribution across the brain, less influenced by extreme high or low dose contributions. The predictive value of $D_{50\%}$ within the brain exceeds that of (near-)maximum dose or gEUD parameters within the brain, brainstem or PVR with high exponents *a*, which weight high-dose voxels more heavily. The gEUD was the most prominent predictor for adult gliomas, with $a = 11$ for the PVR and $a = 9$ for the brain-GTV [34,55] respectively. The results of the current study might indicate a different response to radiation of the brain structures under development. This insight is similar to studies that have analyzed the outcome and risk of brain radionecrosis following stereotactic radiosurgery for cerebral metastases, which identified moderate-to-high dose volumes ($V_{10\ \mathrm{Gy}}$ or $V_{12\ \mathrm{Gy}}$) as key predictors of radionecrosis [56,57]. A reasonable assumption would be that higher energy deposition in the brain, i.e., higher $D_{50\%}$, could lead to a reduction in the repair capacity and thus to a reduction in the (local) threshold dose for IC development.

Beyond dosimetric factors, multimodal treatment strategies—such as combining radiation therapy with chemotherapy, targeted agents, and immunotherapies—can influence the biological tissue response [58] and, therefore, the occurrence of post-treatment ICs. Given the heterogeneity in our cohort, with 25 different chemotherapy agents administered, a specific impact of individual drugs on IC development could not be observed. As these clinical variables were not significant, they were excluded from further multivariate analysis.

Conclusions

In summary, the product of dose and LETd from primary protons—when combined with Gaussian filtering—serves as a key robust predictor for the local IC occurrence within the brain of children. Since LET effects exhibit substantial spatial heterogeneity, they play a more significant role in voxel-wise NTCP models where local variations are preserved. In patient-wise NTCP models, where the influence of local hotspots is diminished due to averaging over larger volumes, $D_{50\%}$

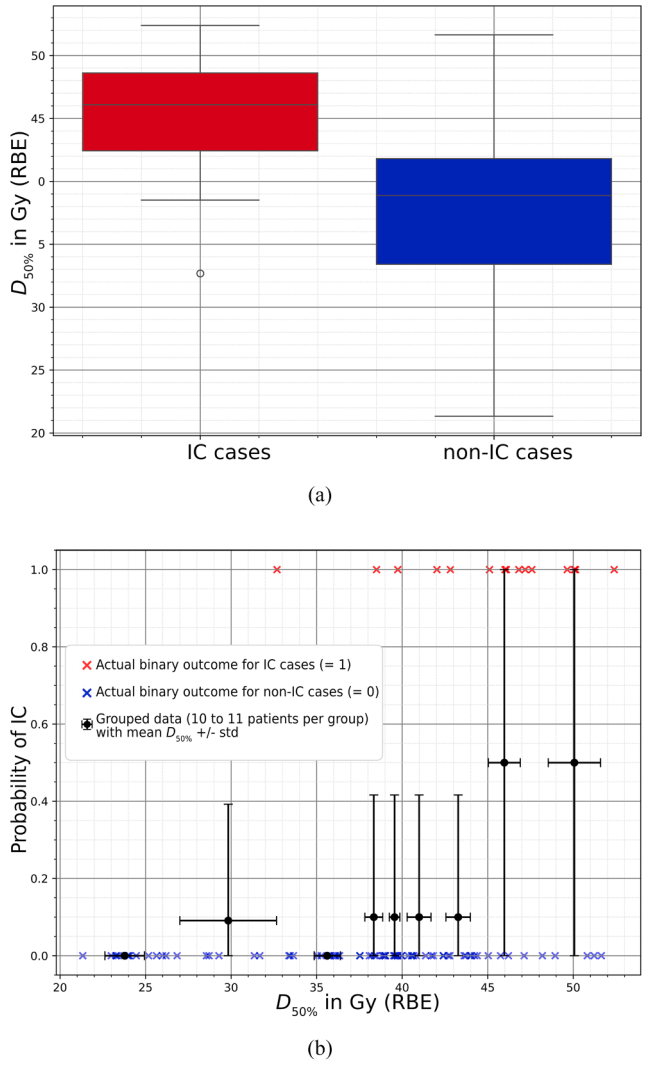

Fig. 2. (a) Boxplot for parameter $D_{50\%}$ (brain) with dose cutoff of 20 Gy (RBE = 1.1), categorized for IC and non-IC patients **(b)** Mean $D_{50\%}$ (brain) with dose cutoff of 20 Gy (RBE = 1.1) with standard deviation (in dose and probability domain) of patients sorted for $D_{50\%}$ (brain) in groups of 10 to 11, plotted against the binary probability of IC occurrence.

appears to be a reliable predictor. These findings hold high clinical relevance for risk assessment and optimizing treatment planning for pediatric CNS tumors treated with protons.

CRediT authorship contribution statement

Feline Heinzelmann: Writing – review & editing, Writing – original draft, Visualization, Validation, Software, Methodology, Investigation, Formal analysis, Data curation, Conceptualization. **Sarah Peters:** Validation, Methodology, Investigation, Data curation, Conceptualization. **Annika Quenzer:** Writing – review & editing, Validation. **Armin Lühr:** Writing – review & editing, Formal analysis, Conceptualization. **Steffen Löck:** Writing – review & editing, Formal analysis, Conceptualization. **Stefanie Schulze Schleithoff:** Writing – review & editing, Project administration, Funding acquisition. **Sabine Frisch:** Writing – review & editing, Project administration, Data curation. **Christian Bäumer:** Writing – review & editing, Supervision, Project administration, Methodology, Investigation, Funding acquisition, Conceptualization. **Beate Timmermann:** Writing – review & editing, Resources, Funding acquisition.

Funding

This research was funded by the Barbara und Hubertus Trettner Stiftung, grant number T0355/36718/2020/sm and by the MERCUR-Stiftung graduate school "Präzisionsprotonentherapie – Praxisbezogene Physik und Chemie an der Schnittstelle zur Medizin" (grant number St-2019–0007).

Additionally, this partnership has received funding from the European Union's "EURATOM" research and innovation program under the 101,061,037 grant agreement.

Declaration of competing interest

The authors declare the following financial interests/personal relationships which may be considered as potential competing interests: The authors declare no conflicts of interest. The funders had no role in study design, data collection, analysis, interpretation, manuscript preparation, or the decision to publish. The author Steffen Löck is an Editor of Radiotherapy and Oncology and was not involved in the editorial review or the decision to publish this article.

Acknowledgments

We would like to thank Christian Hahn for fruitful discussions. The authors gratefully acknowledge the computing time provided on the Linux HPC cluster at Technical University Dortmund (LiDO3), partially funded in the course of the Large-Scale Equipment Initiative by the Deutsche Forschungsgemeinschaft (DFG, German Research Foundation) as project 271512359.

Appendix A. Supplementary material

Supplementary data to this article can be found online at https://doi.org/10.1016/j.radonc.2025.111261.

References

[1] DeNunzio NJ, Yock TI. Modern radiotherapy for pediatric brain tumors. Cancers 2020;12:1533. https://doi.org/10.3390/cancers12061533.
[2] Paganetti H. Proton beam therapy. IOP Publishing; 2016. 10.1088/978-0-7503-1370-4.
[3] Yock TI, Yeap BY, Ebb DH, Weyman E, Eaton BR, Sherry NA, et al. Long-term toxic effects of proton radiotherapy for paediatric medulloblastoma: a phase 2 single-arm study. Lancet Oncol 2016;17:287–98. https://doi.org/10.1016/S1470-2045(15)00167-9.
[4] Gondi V, Yock TI, Mehta MP. Proton therapy for paediatric CNS tumours — improving treatment-related outcomes. Nat Rev Neurol 2016;12:334–45. https://doi.org/10.1038/nrneurol.2016.70.
[5] Mizumoto M, Murayama S, Akimoto T, Demizu Y, Fukushima T, Ishida Y, et al. Long-term follow-up after proton beam therapy for pediatric tumors: a Japanese national survey. Cancer Sci 2017;108:444–7. https://doi.org/10.1111/cas.13140.
[6] Indelicato DJ, Bradley JA, Sandler ES, Aldana PR, Sapp A, Gains JE, et al. Clinical outcomes following proton therapy for children with central nervous system tumors referred overseas. Pediatr Blood Cancer 2017;64:e26654. https://doi.org/10.1002/pbc.26654.
[7] Badiyan SN, Ulmer S, Ahlhelm FJ, Fredh ASM, Kliebsch U, Calaminus G, et al. Clinical and radiologic outcomes in adults and children treated with pencil-beam scanning proton therapy for low-grade glioma. Int J Part Ther 2017;3:450–60. https://doi.org/10.14338/IJPT-16-00031.1.
[8] Indelicato DJ, Bradley JA, Rotondo RL, Nanda RH, Logie N, Sandler ES, et al. Outcomes following proton therapy for pediatric ependymoma. Acta Oncol 2018;57:644–8. https://doi.org/10.1080/0284186X.2017.1413248.
[9] Kahalley LS, Douglas Ris M, Mahajan A, Fatih Okcu M, Chintagumpala M, Paulino AC, et al. Prospective, longitudinal comparison of neurocognitive change in pediatric brain tumor patients treated with proton radiotherapy versus surgery only. Neuro-Oncol 2019;21:809–18. https://doi.org/10.1093/neuonc/noz041.
[10] Jazmati D, Steinmeier T, Khalil DA, Frisch S, Peters S, Schleithoff SS, et al. Feasibility of proton beam therapy for infants with brain tumours: experiences from the prospective KiProReg registry study. Clin Oncol 2021;33:e295–304. https://doi.org/10.1016/j.clon.2021.03.006.
[11] Dutz A, Lühr A, Troost EGC, Agolli L, Bütof R, Valentini C, et al. Identification of patient benefit from proton beam therapy in brain tumour patients based on dosimetric and NTCP analyses. Radiother Oncol 2021;160:69–77. https://doi.org/10.1016/j.radonc.2021.04.008.

[12] Uemura S, Demizu Y, Hasegawa D, Fujikawa T, Inoue S, Nishimura A, et al. The comparison of acute toxicities associated with craniospinal irradiation between photon beam therapy and proton beam therapy in children with brain tumors. Cancer Med 2022;11:1502–10. https://doi.org/10.1002/cam4.4553.

[13] Kralik SF, Ho CY, Finke W, Buchsbaum JC, Haskins CP, Shih C-S. Radiation necrosis in pediatric patients with brain tumors treated with proton radiotherapy. AJNR Am J Neuroradiol 2015;36:1572–8. https://doi.org/10.3174/ajnr.A4333.

[14] Acharya S, Robinson CG, Michalski JM, Mullen D, DeWees TA, Campian JL, et al. Association of 1p/19q codeletion and radiation necrosis in adult cranial gliomas after proton or photon therapy. Int J Radiat Oncol 2018;101:334–43. https://doi.org/10.1016/j.ijrobp.2018.01.099.

[15] Ali FS, Arevalo O, Zorofchian S, Patrizz A, Riascos R, Tandon N, et al. Cerebral radiation necrosis: incidence, pathogenesis, diagnostic challenges, and future opportunities. Curr Oncol Rep 2019;21:1–17. https://doi.org/10.1007/s11912-019-0818-y.

[16] Ritterbusch R, Halasz LM, Graber JJ. Distinct imaging patterns of pseudoprogression in glioma patients following proton versus photon radiation therapy. J Neurooncol 2021;152:583–90. https://doi.org/10.1007/s11060-021-03734-6.

[17] Lütgendorf-Caucig C, Pelak M, Hug E, Flechl B, Surböck B, Marosi C, et al. Prospective analysis of radiation-induced contrast enhancement and health-related quality of life after proton therapy for central nervous system and skull base tumors. Int J Radiat Oncol Biol Phys 2024;118:1206–16. https://doi.org/10.1016/j.ijrobp.2024.01.007.

[18] Winter SF, Gardner MM, Karschnia P, Vaios EJ, Grassberger C, Bussière MR, et al. Unique brain injury patterns after proton vs photon radiotherapy for WHO grade 2-3 gliomas. Oncologist 2024;29. https://doi.org/10.1093/oncolo/oyae195. e1748 e61.

[19] Wang Y-X-J, King AD, Zhou H, Leung S-F, Abrigo J, Chan Y-L, et al. Evolution of radiation-induced brain injury: MR imaging–based study. Radiology 2010;254:210–8. https://doi.org/10.1148/radiol.09090428.

[20] Benghanem S, Mazeraud A, Azabou E, Chhor V, Shinotsuka CR, Claassen J, et al. Brainstem dysfunction in critically ill patients. Crit Care 2020;24:5. https://doi.org/10.1186/s13054-019-2718-9.

[21] Harrabi SB, von Nettelbladt B, Gudden C, Adeberg S, Seidensaal K, Bauer J, et al. Radiation induced contrast enhancement after proton beam therapy in patients with low grade glioma – how safe are protons? Radiother Oncol 2022;167:211–8. https://doi.org/10.1016/j.radonc.2021.12.035.

[22] Niemierko A, Schuemann J, Niyazi M, Giantsoudi D, Maquilan G, Shih HA, et al. Brain necrosis in adult patients after proton therapy: is there evidence for dependency on linear energy transfer? Int J Radiat Oncol Biol Phys 2021;109:109–19. https://doi.org/10.1016/j.ijrobp.2020.08.058.

[23] Strenger V, Lackner H, Mayer R, Sminia P, Sovinz P, Mokry M, et al. Incidence and clinical course of radionecrosis in children with brain tumors. Strahlenther Onkol 2013;189:759–64. https://doi.org/10.1007/s00066-013-0408-0.

[24] Witzmann K, Raschke F, Troost EGC. MR image changes of normal-appearing brain tissue after radiotherapy. Cancers 2021;13:1573. https://doi.org/10.3390/cancers13071573.

[25] Eulitz J, Troost EGC, Raschke F, Schulz E, Lutz B, Dutz A, et al. Predicting late magnetic resonance image changes in glioma patients after proton therapy. Acta Oncol Stockh Swed 2019;58:1536–9. https://doi.org/10.1080/0284186X.2019.1631477.

[26] Bahn E, Bauer J, Harrabi S, Herfarth K, Debus J, Alber M. Late contrast enhancing brain lesions in proton-treated patients with low-grade glioma: clinical evidence for increased periventricular sensitivity and variable RBE. Int J Radiat Oncol Biol Phys 2020;107:571–8. https://doi.org/10.1016/j.ijrobp.2020.03.013.

[27] Bertolet A, Abolfath R, Carlson DJ, Lustig RA, Hill-Kayser C, Alonso-Basanta M, et al. Correlation of LET with MRI changes in brain and potential implications for normal tissue complication probability for patients with meningioma treated with pencil beam scanning proton therapy. Int J Radiat Oncol Biol Phys 2022;112:237–46. https://doi.org/10.1016/j.ijrobp.2021.08.027.

[28] Engeseth GM, He R, Mirkovic D, Yepes P, Mohamed ASR, Stieb S, et al. Mixed effect modeling of dose and linear energy transfer correlations with brain image changes after intensity modulated proton therapy for skull base head and neck cancer. Int J Radiat Oncol 2021;111:684–92. https://doi.org/10.1016/j.ijrobp.2021.06.016.

[29] Giantsoudi D, Sethi RV, Yeap BY, Eaton BR, Ebb DH, Caruso PA, et al. Incidence of CNS injury for a cohort of 111 patients treated with proton therapy for medulloblastoma: LET and RBE associations for areas of injury. Int J Radiat Oncol Biol Phys 2016;95:287–96. https://doi.org/10.1016/j.ijrobp.2015.09.015.

[30] Haas-Kogan D, Indelicato D, Paganetti H, Esiashvili N, Mahajan A, Yock T, et al. National cancer institute workshop on proton therapy for children: considerations regarding brainstem injury. Int J Radiat Oncol Biol Phys 2018;101:152–68. https://doi.org/10.1016/j.ijrobp.2018.01.013.

[31] Garbacz M, Cordoni FG, Durante M, Gajewski J, Kisielewicz K, Krah N, et al. Study of relationship between dose, LET and the risk of brain necrosis after proton therapy for skull base tumors. Radiother Oncol 2021;163:143–9. https://doi.org/10.1016/j.radonc.2021.08.015.

[32] Peeler CR, Mirkovic D, Titt U, Blanchard P, Gunther JR, Mahajan A, et al. Clinical evidence of variable proton biological effectiveness in pediatric patients treated for ependymoma. Radiother Oncol J Eur Soc Ther Radiol Oncol 2016;121:395–401. https://doi.org/10.1016/j.radonc.2016.11.001.

[33] Roberts KW, Tseung HSWC, Eckel LJ, Harmsen WS, Beltran C, Laack NN. Biologic dose and imaging changes in pediatric brain tumor patients receiving spot scanning proton therapy. Int J Radiat Oncol Biol Phys 2019;105:664–73. https://doi.org/10.1016/j.ijrobp.2019.06.2534.

[34] Eulitz J, Troost EGC, Klünder L, Raschke F, Hahn C, Schulz E, et al. Increased relative biological effectiveness and periventricular radiosensitivity in proton therapy of glioma patients. Radiother Oncol 2023;178. https://doi.org/10.1016/j.radonc.2022.11.011.

[35] Vestergaard A, Kallehauge JF, Muhic A, Carlsen JF, Dahlrot RH, Lukacova S, et al. Mixed effect model confirms increased risk of image changes with increasing linear energy transfer in proton therapy of gliomas. Radiother Oncol 2025. https://doi.org/10.1016/j.radonc.2025.110716.

[36] Wang JH, Oglesby R, Tran A, Guryildirim M, Miller M, Sheikh K, et al. The association of linear energy transfer and dose with radiation necrosis after pencil beam scanning proton therapy in pediatric posterior fossa tumors. Int J Radiat Oncol 2025;121:1219–28. https://doi.org/10.1016/j.ijrobp.2024.11.086.

[37] Handeland AH, Indelicato DJ, Fjæra LF, Ytre-Hauge KS, Pettersen HES, Muren LP, et al. Linear energy transfer-inclusive models of brainstem necrosis following proton therapy of paediatric ependymoma. Phys Imaging Radiat Oncol 2023;27. https://doi.org/10.1016/j.phro.2023.100466.

[38] Hahn C, Ödén J, Dasu A, Vestergaard A, Fuglsang Jensen M, Sokol O, et al. Towards harmonizing clinical linear energy transfer (LET) reporting in proton radiotherapy: a European multi-centric study. Acta Oncol 2022;61:206–14. https://doi.org/10.1080/0284186X.2021.1992007.

[39] Wedenberg M, Lind BK, Hårdemark B. A model for the relative biological effectiveness of protons: the tissue specific parameter α/β of photons is a predictor for the sensitivity to LET changes. Acta Oncol Stockh Swed 2013;52:580–8. https://doi.org/10.3109/0284186X.2012.705892.

[40] Carabe A, España S, Grassberger C, Paganetti H. Clinical consequences of relative biological effectiveness variations in proton radiotherapy of the prostate, brain and liver. Phys Med Biol 2013;58:2103–17. https://doi.org/10.1088/0031-9155/58/7/2103.

[41] McNamara AL, Schuemann J, Paganetti H. A phenomenological relative biological effectiveness (RBE) model for proton therapy based on all published in vitro cell survival data. Phys Med Biol 2015;60:8399–416. https://doi.org/10.1088/0031-9155/60/21/8399.

[42] Peeler CR. Assessing the Potential Clinical Impact of Variable Biological Effectiveness In Proton Radiotherapy. The University of Texas; 2016.

[43] Rørvik E, Fjæra LF, Dahle TJ, Dale JE, Engeseth GM, Stokkevåg CH, et al. Exploration and application of phenomenological RBE models for proton therapy. Phys Med Biol 2018;63:185013. https://doi.org/10.1088/1361-6560/aad9db.

[44] Unkelbach J, Botas P, Giantsoudi D, Gorissen BL, Paganetti H. Reoptimization of intensity modulated proton therapy plans based on linear energy transfer. Int J Radiat Oncol Biol Phys 2016;96:1097–106. https://doi.org/10.1016/j.ijrobp.2016.08.038.

[45] Grassberger C, Paganetti H. Elevated LET components in clinical proton beams. Phys Med Biol 2011;56:6677–91. https://doi.org/10.1088/0031-9155/56/20/011.

[46] Lambrecht M, Eekers DBP, Alapetite C, Burnet NG, Calugaru V, Coremans IEM, et al. Radiation dose constraints for organs at risk in neuro-oncology; the European particle therapy network consensus. Radiother Oncol 2018;128:26–36. https://doi.org/10.1016/j.radonc.2018.05.001.

[47] Peters S, Frisch S, Stock A, Merta J, Bäumer C, Blase C, et al. Proton beam therapy for pediatric tumors of the central nervous system—experiences of clinical outcome and feasibility from the KiProReg study. Cancers 2022;14:5863. https://doi.org/10.3390/cancers14235863.

[48] Fouladi M, Chintagumpala M, Laningham FH, Ashley D, Kellie SJ, Langston JW, et al. White matter lesions detected by magnetic resonance imaging after radiotherapy and high-dose chemotherapy in children with medulloblastoma or primitive neuroectodermal tumor. J Clin Oncol 2004;22:4551–60. https://doi.org/10.1200/JCO.2004.03.058.

[49] Mailhot R, Rotondo R, Murphy E, Caruso PA, Fullerton B, Tarbell NJ, et al. A consensus atlas for whole ventricular irradiation for pediatric germ cell tumors: survey results and guidelines. Int J Radiat Oncol Biol Phys 2012;84:S65.

[50] De Marzi L, Feuvret L, Boulé T, Habrand J-L, Martin F, Calugaru V, et al. Use of gEUD for predicting ear and pituitary gland damage following proton and photon radiation therapy. Br J Radiol 2015;88:20140413. https://doi.org/10.1259/bjr.20140413.

[52] Li G, Yin C, Zhang C, Xue B, Yang Z, Li Z, et al. Spatial distribution of supratentorial diffuse gliomas: a retrospective study of 990 cases. Front Oncol 2023;13:1098328. https://doi.org/10.3389/fonc.2023.1098328.

[53] Lühr A, Wagenaar D, Eekers DBP, Glimelius L, Habraken SJM, Harrabi S, et al. Recommendations for reporting and evaluating proton therapy beyond dose and constant relative biological effectiveness. Phys Imaging Radiat Oncol 2025;33. https://doi.org/10.1016/j.phro.2024.100692.

[54] Heuchel L, Hahn C, Pawelke J, Sørensen BS, Dosanjh M, Lühr A. Clinical use and future requirements of relative biological effectiveness: survey among all European proton therapy centres. Radiother Oncol 2022;172:134–9. https://doi.org/10.1016/j.radonc.2022.05.015.

[55] Niyazi M, Niemierko A, Paganetti H, Söhn M, Schapira E, Goldberg S, et al. Volumetric and actuarial analysis of brain necrosis in proton therapy using a novel mixture cure model. Radiother Oncol 2020;142:154–61. https://doi.org/10.1016/j.radonc.2019.09.008.

[56] Blonigen BJ, Steinmetz RD, Levin L, Lamba MA, Warnick RE, Breneman JC. Irradiated volume as a predictor of brain radionecrosis after linear accelerator stereotactic radiosurgery. Int J Radiat Oncol Biol Phys 2010;77:996–1001. https://doi.org/10.1016/j.ijrobp.2009.06.006.

[57] Minniti G, Clarke E, Lanzetta G, Osti MF, Trasimeni G, Bozzao A, et al. Stereotactic radiosurgery for brain metastases: analysis of outcome and risk of brain radionecrosis. Radiat Oncol 2011;6:48. https://doi.org/10.1186/1748-717X-6-48.
[58] Paganetti H. Mechanisms and review of clinical evidence of variations in relative biological effectiveness in proton therapy. Int J Radiat Oncol Biol Phys 2022;112:222–36. https://doi.org/10.1016/j.ijrobp.2021.08.015.
[59] Bojaxhiu B, Ahlhelm F, Walser M, Placidi L, Kliebsch U, Mikroutsikos L, et al. Radiation necrosis and white matter lesions in pediatric patients with brain tumors treated with pencil beam scanning proton therapy. Int J Radiat Oncol Biol Phys 2018;100:987–96. https://doi.org/10.1016/j.ijrobp.2017.11.037.

Further reading

[51] Gentile MS, Yeap BY, Paganetti H, Goebel CP, Gaudet DE, Gallotto SL, et al. Brainstem injury in pediatric patients with posterior fossa tumors treated with proton beam therapy and associated dosimetric factors. Int J Radiat Oncol Biol Phys 2018;100:719–29. https://doi.org/10.1016/j.ijrobp.2017.11.026.